ACTA PHYSICA POLONICA A No. 5 Vol. **147** (2025)

Comprehensive Study of Electronic, Thermal and Magnetic Properties of Bilayer Phosphorene Nanoribbons

S. Fathi, M. Zare*, A. Avazpour and P. Zamani

Physics Department, Yasouj University, Yasouj 75918-74831, Iran

Received: 31.01.2025 & Accepted: 11.04.2025

Doi: 10.12693/APhysPolA.147.408

*e-mail: mzare@yu.ac.ir

The electronic, thermal, and magnetic properties of zigzag bilayer phosphorene nanoribbons are investigated using the Green's function approach within the tight-binding model. These materials exhibit a fully reversible metal–to–semiconductor (or insulator) phase transition when subjected to a perpendicular electric field. In the absence of interlayer coupling, the band structure of zigzag bilayer phosphorene nanoribbons features two non-tilted Dirac cones. However, when interlayer coupling is introduced, two tilted Dirac cones emerge at the crossing points, exhibiting the lack of electron–hole symmetry. Significant tuning of the Fermi velocity and effective mass is achieved by adjusting the external bias voltage. At specific critical voltages, electron localization behavior is observed. Thermal and magnetic properties of zigzag bilayer phosphorene nanoribbons are also studied using the continuum model. Both the Pauli paramagnetic susceptibility and electronic heat capacity of zigzag bilayer phosphorene nanoribbons are found to be tunable by modifying the ribbon width and applying an electric field. The demonstrated potential for simultaneous control of thermal and magnetic properties through an experimentally feasible electric field paves the way for developing novel thermomagnetic devices based on zigzag bilayer phosphorene nanoribbons. Additionally, the flexibility of band tunability in zigzag bilayer phosphorene nanoribbons enhances their potential applications in next-generation optoelectronic nanodevices.

topics: zigzag bilayer phosphorene nanoribbon (ZBLPNR), Pauli paramagnetic susceptibility (PPS), heat capacity (HC), Fermi velocity

1. Introduction

The miniaturization of modern electronic devices has been attracting increasing attention in recent years in the development of low-dimensional materials. Two-dimensional (2D) materials have garnered enormous interest due to their exotic electronic properties and potential applications in nanoelectronics, spintronics, and optical materials. Since its isolation in 2014 [1, 2], phosphorene, the most stable phosphorus allotrope with a layered structure, has been the subject of intense study in the fields of optoelectronics [3, 4], magneto-optics [5–7], and thermoelectrics [8].

Within a phosphorene single layer, each phosphorus atom forms covalent bonds with three adjacent phosphorus atoms, creating a folded honeycomb lattice. Additionally, each atom possesses a non-bonding lone pair of electrons, which contributes to the stabilization of the geometric distortion [9] and facilitates interlayer van der Waals (vdW) interactions [10, 11]. The puckered crystal structure of phosphorene, resulting from sp^3 hybridization [12–14], leads to strong anisotropy in the energy dispersion and, consequently, in the effective mass of the electrons. This anisotropy influences the thermal, electrical, and optical properties of phosphorene, while also providing high sensitivity in strain engineering [15, 16].

By exploiting quantum confinement effects, the direct bandgap in phosphorene can be tuned by varying the number of layers. More effectively, it can also be adjusted by applying an electric field and strain, bridging the gap between graphene and other 2D materials [17–20]. In analogy with graphene nanoribbons, further reduction in the dimensionality of 2D black phosphorus (BP) in the form of phosphorene nanoribbons (PNRs) compensates for the lack of a bandgap in the extended 2D material, which is fundamental to the development of 2D nanoelectronics [21–27]. In addition to that, compared to 2D phosphorene sheets, quasi-one-dimensional phosphorene nanoribbons provide greater tunability of structural, electrochemical, and electronic properties [28, 29]. Therefore, insights into the electronic, magnetic, and thermal properties of PNRs are critical for designing next-generation magnetoelectric and optoelectronic devices based on phosphorene nanoribbons.

The electronic, optical, and transport properties of PNRs are heavily influenced by quantum confinement and edge morphology [21–27]. Notably, the presence of topological edge states in BP nanoribbons [25, 27] enhances optical absorption [30–32], offering advantages for photocatalytic and energy applications [30].

The effective mass and Fermi velocity, two excellent first-order descriptors in real systems, serve as a convenient measure of the electronic band structure, characterizing the density of states and electron transport based on the common free electron approximation [33]. These two characteristics are critical parameters in conventional Fermi liquid theory, governing observable quantities in electronic systems. Various methods, including electron concentration modification [34, 35], strain engineering [36, 37], electric fields [38], curvature of the sample [39], periodic potentials [40], substrate modifications [41], and placing metallic planes near the material [42, 43], have been proposed to modulate these parameters in 2D materials. The Fermi velocity modulation can control the energy gap [44], the Fano factor [45], and the spin [46] and valley [47] transport in graphene. However, the Fermi velocity can also be used to create electron guides [42, 43] and bound states [48] in graphene. In recent years, the potential for designed modifications to alter the effective mass and Fermi velocity, which are the most important transport quantities for the practical application of nanoribbons, has been explored. Thus, modifying and tuning these key parameters in nanoribbons is a pivotal aspect of optimizing their performance.

However, despite numerous attempts to find an effective and efficient method for modulating the Fermi velocity and effective mass in 2D materials, this issue remains unresolved in few-layer phosphorene nanoribbons. As we will demonstrate in the next section, this is feasible and can be implemented since the effective mass and Fermi velocity become field-dependent and can therefore be tuned by adjusting the external bias voltage.

Motivated by the recent experimental synthesis of few-layer phosphorene nanoribbons [24, 29, 49], we have demonstrated a new avenue to control the Fermi velocity and effective mass of carriers in zigzag bilayer phosphorene nanoribbons (ZBLPNRs). Prior to this, we also obtained the electronic properties of ZBLPNRs in the presence of gate voltage. The band gap modulation of ZBLPNRs by the ribbon width and perpendicular electric field is investigated. We illustrate how one can isolate the edge state from the bulk contribution by tuning the external gate potential. Since the layer number significantly affects the physical properties of 2D black phosphorus multilayers, it is of both fundamental and practical interest to study the effect of interlayer coupling on these properties. We explain how interlayer coupling influences electronic structure characterizations, specifically the energy band gap, Fermi velocity, and effective mass of carriers in biased BLPNRs.

Moreover, in the second part of the paper, the interest in studying the thermal and magnetic properties of low-dimensional materials within scientific and engineering communities [50] compels us to adopt a comparative perspective to identify both the orbital magnetic susceptibility and heat capacity (HC) in ZBLPNRs, employing a tight-binding approach alongside the conventional Green's function technique. Here, we focus on how the orbital magnetic susceptibility and heat capacity in ZBLPNRs are modified by varying the perpendicular electric field due to changes in the band structure, which can effectively control thermal and magnetic properties via an electric field. Additionally, we demonstrate that by altering the width of the phosphorene ribbons, one can significantly change both the orbital magnetic susceptibility and heat capacity of ZBLPNRs.

The remainder of this work is structured as follows: In Sect. 2, we present a tight-binding model Hamiltonian for biased bilayer phosphorene and calculate the electronic band structure and density of states of ZBLPNR under a vertical electric field. We then explain the method used to calculate the orbital magnetic susceptibility and heat capacity of ZBLPNRs, employing the Green's function technique. Following this, we discuss our numerical results for the proposed ZBLPNR in the presence of a perpendicular electric field. Finally, in Sect. 3, we summarize our findings.

2. Theory and model

To understand the thermal and magnetic properties of gated bilayer phosphorene, we first consider its electronic structure. In the following section, we present a tight-binding (TB) description of the electronic structure of bilayer phosphorene subjected to a perpendicular electric field.

Since Bernal stacking (also known as AB stacking) is the most energetically stable configuration of bilayer phosphorene [51, 52], we examine an AB-stacked ZBLPNR as illustrated in Fig. 1. The TB Hamiltonian for electrons, incorporating intralayer and interlayer hoppings between the phosphorus atoms in ZBLPNR under a uniform perpendicular electric field, is expressed as follows [53–55]

$$H = \sum_i V_i \; c_i^\dagger c_i + \sum_{i \neq j} t_{ij}^{\parallel} \; c_i^\dagger c_j + \sum_{i \neq j} t_{ij}^{\perp} \; c_i^\dagger c_j. \tag{1}$$

The first term in (1) relates to the sublattice chemical potential induced by a gate voltage, where V_i represents the on-site energy at site i. The second term accounts for the hopping of nearest neighbors in intralayer interactions among phosphorus atoms, while the third term describes hopping between phosphorus atoms in different layers.

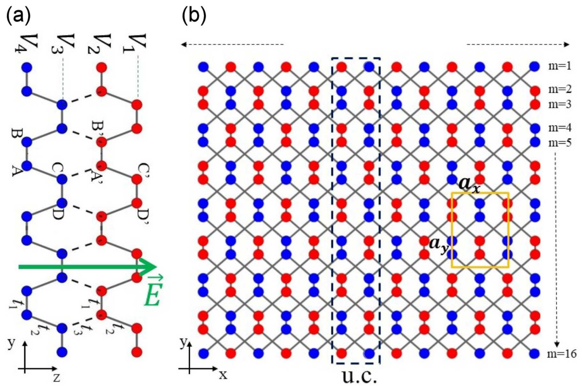

Fig. 1. Schematic illustration of zigzag bilayer black phosphorus nanoribbon with $M = 16$ — side view (panel a) and top view (panel b) — in the presence of a perpendicular electric field $\boldsymbol{E}$. The positions of the phosphorus atoms located in the bottom and top layers are presented by blue and red circles, respectively. The solid rectangle represents the unit cell of bulk bilayer phosphorene with the lattice constants a_x and a_y, and the dashed rectangle denotes the unit cell (u.c.) in the calculation of the tight-binding model of the nanoribbon.

Further, $c_i^\dagger$ and c_j, respectively, are the creation and annihilation operators of electrons at sites i and j, and $t_{ij}^{\parallel}$ ($t_{ij}^{\perp}$) is the intralayer (interlayer) hopping energy between sites i and j, and the summation runs over entire nanoribbon lattice sites.

Here, $t_1 = -1.21$ eV and $t_2 = 3.18$ eV are two in-plane hopping terms, and $t_3 = 0.22$ eV is the interlayer hopping term [53] (as shown in Fig. 1). In the presence of a perpendicular electric field, the four atomic sublayers in BLPNR gain different on-site potentials, including: $V_1 = (1/2+\epsilon)V$, $V_2 = (1/2-\epsilon)V$, $V_3 = (-1/2+\epsilon)V$, and $V_4 = (-1/2-\epsilon)V$, where $V = e\,E\,d$ is the potential energy difference between the top and bottom phosphorene layers, with e being the elementary charge, E denoting the electric field strength, and d representing the distance between its sublayers, and $\epsilon = 0.202$ is the linear scaling factor that accounts for the sublayer dependence electrostatic potential [56].

It should be noted that for a typical value of $V = 1$ eV, a rough estimate obtained using the relation $V = e\,E\,d$ (where $d = 10.57$ Å is the distance between the outermost layers of the bilayer (BL) phosphorene structure [52] or in other words, the interlayer separation of the BL phosphorene), gives a corresponding electric field E as high as $E = 0.09$ eV/Å. There have been several theoretical studies on few-layer phosphorene that have considered the external electric fields of this magnitude or even larger [52–56]. It is known that generating a huge electric field is a big challenge for experiments and probably can be done by ionic gating and/or polarized interfaces, as proposed in [57]. Of course, it is interesting that extreme bias voltages (from -25 to 25 V) have already been used in black phosphorous thin films [58]. It is worth mentioning that in the tight-binding Hamiltonian (1), the screening of the external potential is neglected. If readers want to learn more about the screening of the external potential in BLPNRs, we refer to [59].

In Fig. 1, we sketch a BLPNR with zigzag edges. The conventional unit cell of a bulk BL phosphorene (solid-orange rectangle) consists of eight atoms with the lattice constants $a_x = 3.3$ Å and $a_y = 4.63$ Å in x (zigzag) and y (armchair) directions, respectively. Here, the unit cell used in the tight-binding calculations of the ZBLPNR (dashed rectangle) is also indicated. The respective unit cell width is a_x.

To study the band structure properties provided by our tight-binding model, we find its $\boldsymbol{k}$-space forms as

$$H(\boldsymbol{k}) = \sum_{\boldsymbol{k}} \psi_{\boldsymbol{k}}^\dagger\, H_k\, \psi_{\boldsymbol{k}}. \tag{2}$$

In this ribbon geometry, the electron wave vector along the x-direction (k_x) serves as a good quantum number. Thus, by applying Bloch's theorem and performing a Fourier transformation along the x-direction, the $\boldsymbol{k}$-dependent Hamiltonian of the nanoribbon can be expressed as follows

$$H_k = H_{00} + H_{01}\,\mathrm{e}^{-\mathrm{i}\,k_x a_x} + H_{01}^\dagger\,\mathrm{e}^{\mathrm{i}\,k_x a_x}, \tag{3}$$

where H_{00} is the unit cell (intra-unit cell) Hamiltonian and H_{01} describes the coupling (inter-unit cell) Hamiltonian between neighboring cells, based on the real space tight-binding model given by (1).

2.1. Tight-binding model for bilayer phosphorene nanoribbon

In the tight-binding description of bilayer black phosphorus, one now has to consider 8 sublattices, which we label A, B, C, and D for the lower layer and A', B', C', and D' for the upper one (see Fig. 1). Therefore, the Hamiltonian for bilayer phosphorene, acting on the spinors $\Psi = [\phi_A\ \phi_B\ \phi_D\ \phi_C\ \phi'_A\ \phi'_B\ \phi'_D\ \phi'_C]^{\mathrm{T}}$, is a $\boldsymbol{k}$-dependent eight-dimensional matrix

$$H(\boldsymbol{k}) = \begin{pmatrix} H_{\mathrm{B}}(\boldsymbol{k}) & H_{\mathrm{BT}}(\boldsymbol{k}) \\ H_{\mathrm{TB}}(\boldsymbol{k}) & H_{\mathrm{T}}(\boldsymbol{k}) \end{pmatrix}, \tag{4}$$

where $H_{\mathrm{B(T)}}(\boldsymbol{k})$ and $H_{\mathrm{BT(TB)}}(\boldsymbol{k})$ are four-dimensional matrices that describe intra- and interlayer hopping matrices within the bottom and top phosphorene layers. The intra-layer and inter-layer Hamiltonian matrices in momentum space can be written, respectively, as

$$H_{\mathrm{B}}(\boldsymbol{k}) = H_{\mathrm{T}}(\boldsymbol{k}) =$$

$$\begin{pmatrix} u_A & t_{AB}(\boldsymbol{k}) & t_{AD}(\boldsymbol{k}) & t_{AC}(\boldsymbol{k}) \\ t_{AB}(\boldsymbol{k})^* & u_B & t_{AC}(\boldsymbol{k})^* & t_{AD}(\boldsymbol{k}) \\ t_{AD}(\boldsymbol{k}) & t_{AC}(\boldsymbol{k}) & u_D & t_{AB}(\boldsymbol{k}) \\ t_{AC}(\boldsymbol{k})^* & t_{AD}(\boldsymbol{k}) & t_{AB}(\boldsymbol{k})^* & u_C \end{pmatrix} \tag{5}$$

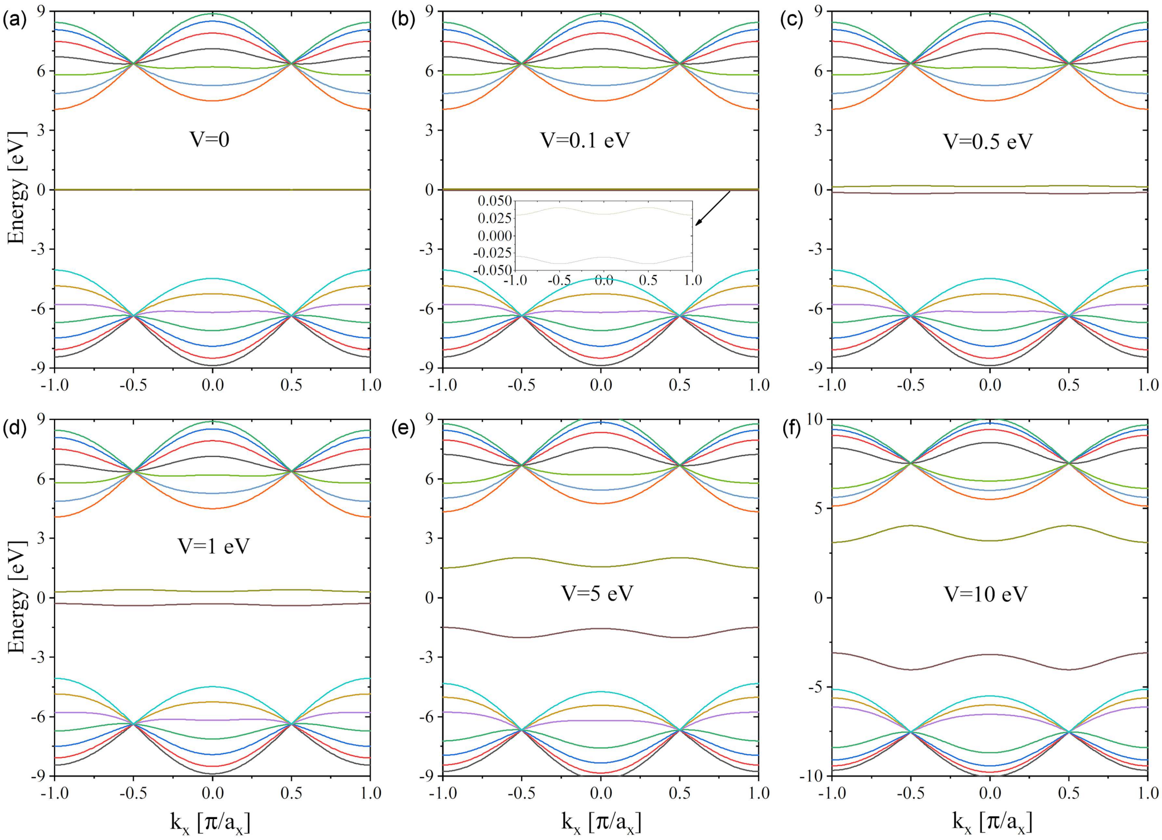

Fig. 2. The one-dimensional (1D) band structures of the system in Fig. 1 with (a–f) different external electric potential V, in which k_x is the wave vector parallel to the zigzag direction.

(with eigenvectors given by $[\phi_A\ \phi_B\ \phi_D\ \phi_C]^{\mathrm{T}}$ and $u_{A,B,C,D}$ representing the on-site energies, with the A–C subscripts denoting the four sublattice labels shown in Fig. 1) and

$$H_{\mathrm{BT}}(\boldsymbol{k}) = \begin{pmatrix} 0 & 0 & t_{AD'}(\boldsymbol{k}) & t_{AC'}(\boldsymbol{k}) \\ 0 & 0 & t_{BD'}(\boldsymbol{k}) & t_{BC'}(\boldsymbol{k}) \\ 0 & 0 & 0 & 0 \\ 0 & 0 & 0 & 0 \end{pmatrix}, \tag{6}$$

including the couplings between sites located in two decoupled layers, i.e., lattice sites A, B, C', and D'. A simple calculation shows that the k-dependent intra-layer (t_{AB}, t_{AC}, and t_{AD}) and inter-layer ($t_{AD'}$ and $t_{AC'}$) coupling contributions can be found as

$$\begin{aligned} & t_{AB}(\boldsymbol{k}) = 2t_1\, \mathrm{e}^{\mathrm{i}\, k_y/2} \cos\left(\sqrt{3}k_x/2\right) \\ & t_{AC}(\boldsymbol{k}) = t_2\, \mathrm{e}^{-\mathrm{i}\, k_y}, \quad t_{AD}(\boldsymbol{k}) = 0, \quad t_{AD'}(\boldsymbol{k}) = 0, \\ & t_{AC'}(\boldsymbol{k}) = 2t_3\, \mathrm{e}^{-\mathrm{i}\, k_y} \cos\left(\sqrt{3}k_x\right). \end{aligned} \tag{7}$$

By identifying the point group symmetry of the phosphorene layer (which is an orthorhombic structure with point group C_{2h}), its 2-band model Hamiltonian is given by $H_2 = \sum_{\boldsymbol{k}} c^{\dagger}(\boldsymbol{k}) \hat{H}_2(\boldsymbol{k}) c(\boldsymbol{k})$ with

$$\hat{H}_{2-\mathrm{band}} = \begin{pmatrix} 0 & f_1 + f_2 \\ f_1^* + f_2^* & 0 \end{pmatrix}, \tag{8}$$

in which $f_1 = t_{AB}(\boldsymbol{k})$ and $f_2 = t_{AC}(\boldsymbol{k})$), which acts on the spinors

$$\Psi = \frac{1}{2} \begin{pmatrix} \phi_A + \phi_D \\ \phi_B + \phi_C \end{pmatrix}. \tag{9}$$

It is easy to show that the energy spectrum of this 2-band model Hamiltonian reads

$$E = \sqrt{t_2^2 + 4\left[t_1^2 + t_1 t_2 \cos\left(\frac{3}{2}k_x\right)\right] \cos\left(\frac{\sqrt{3}}{2}k_y\right)}, \tag{10}$$

which implies the existence of two Dirac cones at

$$k_x = \pm \arctan\left(\frac{\sqrt{t_2^2 - 4t_1^2}}{t_2}\right), \qquad k_y = 0, \tag{11}$$

in 1D-ZBLPNR, for $|t_2| > 2|t_1|$.

We begin by presenting the band structure of ZBLPNRs. Here, we investigate the evolution of the band structure of ZBLPNRs under the influence of a perpendicular electric field. Some of these calculations can be found in paper [60], but the analysis we present serves as an important guide for the subsequent discussion of the thermal and magnetic properties of ZBLPNR.

The calculated band structures of ZBLPNRs are shown in Fig. 2. Interestingly, the ZBLPNR exhibits two nearly degenerate edge states close to the Fermi energy $E_{\mathrm{F}} = 0$, which are entirely detached from the bulk bands. These two edge states are quite similar to the corresponding modes of the zigzag monolayer phosphorene nanoribbons [25, 61–64]. Moreover, the band degeneracy is lifted due to sublattice-symmetry breaking, and a band gap can be easily created by applying an electric field perpendicular to the structure. The flexible band tunability of ZBLPNR enhances its potential applications in next-generation optoelectronic nanodevices.

The properties of the edge states in ZBLPNRs are fundamentally different from those in other 2D zigzag nanoribbons. In comparison with ZBLPNR and monolayer zigzag phosphorene nanoribbon (ZPNR), in the band structure of the graphene and silicene nanoribbons, the edge modes merge into the bulk bands at the two Dirac points. As recently addressed by Ezawa [25], the origin of this decoupled nature of the flat edge modes is the presence of two out-of-plane zigzag chains coupled by a relatively strong hopping parameter. Generally, the edge states projecting to the outermost atoms of a ribbon in real space are near the Fermi level E_{F} [25, 65].

As previously noted in [60, 66], the energy gap increases linearly with the applied electric field, while a band gap, in which a pair of midgap bands is completely separated from the bulk bands, is consistently observed [67–69]. The position of the midgap bands in the energy diagram of ZBSNRs can be altered by applying a perpendicular electric field. In the results presented here, the controllable phosphorus nanoribbons show promise in modulating the midgap energy bands for the next generation of semiconductor electronic devices [67–69].

The band gap energy of ZBSNRs is highly dependent on the applied electric potential, allowing for the engineering of the electronic properties of ZBSNRs with desired characteristics through the adjustment of the external electric field. This indicates that a complete and fully reversible metal–to–semiconductor (or insulator) transition can be observed by tuning the external electric potential, which can be readily achieved experimentally.

It is worth mentioning that the tight-binding model Hamiltonian used in this work to calculate the band structure of bilayer phosphorene nanoribbons is based on the three-parameter tight-binding approximation, while there is a seminal paper that analyzes the band structure and electronic transport of black phosphorus nanoribbons using the five-parameter TB approximation [62]. If the readers are interested in learning more about the TB models of phosphorene nanoribbons, please refer to the work of Taghizadeh Sisakht et al. [62] for a systematic study. Our findings are in agreement with the results presented in [62], where it was shown that semiconducting behavior is predicted for PNRs and that an insulator–metal transition can be expected when a transverse electric field is applied. Taghizadeh Sisakht et al. [62] also showed that in zPNRs, an external transverse electric field can remove the overlap between quasi-flat bands. Moreover, it was also reported that the opposite sign of the two hopping integrals in the phosphorene TB model is the cause of the creation of a relativistic band dispersion along the armchair direction.

However, it is crucial to note that developing and implementing straightforward methods to modulate the tight-binding hoppings is essential for enhancing the performance of 2D electronic devices [70–83]. The tight-binding hoppings can potentially be adjusted and understood through variations in lattice parameters, atomic mass, strain effects, pressure, spin-orbit coupling, and more [70]. This tunability may broaden the range of optical, mechanical, and electrical properties of these 2D materials for device applications [71, 72]. It has been demonstrated that the strengths of different hopping parameters can be relatively easily tuned by incorporating ultracold fermionic atoms in optical lattices, using a dimerization term defined by altering the hopping amplitude [73]. By modifying the hopping integrals between atoms, the Dirac cone can be gapped, transforming it into a 1D topological insulator or a trivial insulator [73, 74].

Among the tight-binding hopping integrals in two-dimensional van der Waals heterostructures, tuning and exploiting interlayer coupling can be effectively achieved through various means. However, understanding how to precisely control the local interlayer coupling remains an ongoing challenge that must be addressed experimentally. A wide array of methods and applications for tuning interlayer coupling has been developed. Meng et al. [75, 76] describe a straightforward method to modulate interlayer coupling by adsorbing single-molecule magnets onto twisted bilayer graphene. They demonstrated that the magnitude of interlayer coupling can be enhanced through the adsorption of single-molecule magnets on twisted bilayer graphene [77]. Furthermore, it has been shown that the magnitude of interlayer coupling can be adjusted by the local coverage density of molecular adsorption [77]. Zhu et al., in a recent study [78], proposed a simple, efficient, and well-controlled technique to enhance interlayer interaction in heterostructures, where the interlayer interaction is tuned from weak to strong coupling via laser irradiation. Moreover, extensive analysis has been conducted for experimentally controllable interlayer coupling to achieve strong values in ultracold atom systems [79]. Recently, in a similar study [79], it was shown that the orbital susceptibility of T-graphene reveals a diamagnetic–to–paramagnetic phase transition by tuning the hopping parameters.

On the other hand, the sign of the interlayer coupling is also significant, as considering a negative or positive value for hopping energy leads to dramatic

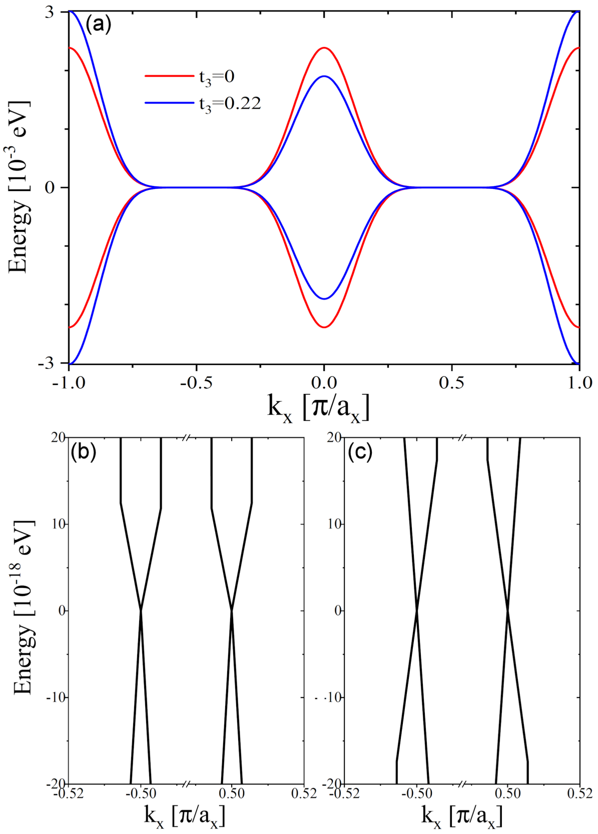

Fig. 3. (a) The highest valence band (HVB) and the lowest conduction band (LCB) for ZBLPNR with $M = 16$, in the absence of the electric field ($V = 0$) and with ($t_3 = 0$, red curve) and without ($t_3 = 0.22$ eV, blue curve) the interlayer coupling. Panels (b) and (c) show a zoomed view of panel (a) for the highest and lowest bands near the zero Fermi energy in the vicinity of the high symmetry points $k_x = \pm\pi/2$.

differences in physical characteristics [81, 82]. For instance, a negative hopping case results in an insulator-like self-energy, while positive hopping leads to metallic behavior [83]. Thus, the sign of the hopping integral plays a crucial role in determining its electronic and magnetic properties. So, given the significance of the varying interlayer coupling in vdW-coupled 2D materials, it is essential to investigate the evolution of interlayer coupling in bilayer phosphorene nanoribbons. As will be demonstrated, the interlayer interaction can substantially alter both the electronic and magnetic properties of ZBLPNRs.

However, to explore the occurrence of Dirac cones in the electronic band structure of the system, in Fig. 3 we show the highest valence band (HVB) and lowest conduction band (LCB) near the Fermi energy ($E_F = 0$) for a ZBLPNR. In Fig. 3a, the HVB and LCB for the ZBLPNR with $M = 16$ are shown in the absence of the electric field ($V = 0$), with ($t_3 = 0$, red curve) and without ($t_3 = 0.22$ eV, blue curve) the interlayer coupling. Panels (b) and (c) show a zoomed view of panel (a) for the highest and lowest bands near zero Fermi energy in the vicinity of the high symmetry points $k_x = \pm\pi/2$. As depicted in Fig. 3b and c, the band structure of ZBLPNR exhibits two Dirac cones at zero Fermi energy. These gapless edge states in ZBLPNRs arise from the original edge states. It is important to note that in the presence of t_3 (see Fig. 3b), the low-energy band structure of a ZBLPNR has two tilted Dirac cones, while in the absence of t_3 (see Fig. 3c), the two Dirac cones are non-tilted. Besides, the bands above and below the Fermi level are not symmetric even near the Dirac point — there is no electron–hole symmetry in the band structures for both limits of t_3. We find that as t_3 is increased, the Dirac cones become more tilted, while, as it is decreased, the Dirac cones become less tilted and shift continuously to the point $k_x = \pm 3\pi/2$, and finally disappear. Moreover, near the zero Fermi energy, the bands above and below the Fermi level are not symmetric, which leads to particle–hole asymmetry. The tilted Dirac cone electronic structure is similar to that of 8-*Pmmn* borophene [84] and graphene under uniaxial strain [85].

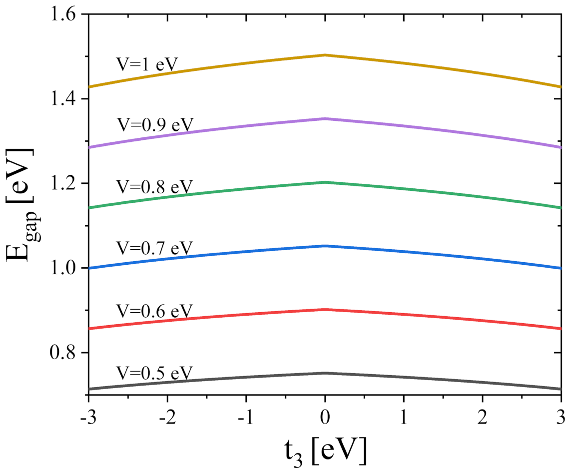

Fig. 4. Energy gap of bilayer phosphorene nanoribbons with widths $M = 12$ and 24 as a function of the interlayer hopping parameter t_3 for various bias voltage V.

It is instructive to study the changes in the band structure of the 1D ZBLPNRs, especially the energy gap of the ZBLPNRs, by changing the interlayer hopping in a continuous manner, with t_1 and t_2 being fixed. Figure 4 shows the energy gap E_g of the ZBLPNRs with widths $M = 12$ and 24 as a function of the interlayer coupling t_3. As can be seen, for a fixed potential, the energy gap decreases as the interlayer coupling increases. However, including the interaction term (considering the van der Waals interaction between layers), the energy gap decreases linearly with increasing interlayer coupling.

Here, we study the influence of finite-size effects on the electronic band structure of BLPNRs by plotting the density of states (DOS). The electronic density of states at energy E can be calculated by means of tracing over the imaginary part of Green's function $\mathbb{G}(\boldsymbol{k}, E)$ as follows

$$D(E) = -\frac{1}{\pi N_c} \sum_{\alpha=1}^{M} \sum_{\boldsymbol{k}} \operatorname{Im}\left[\mathbb{G}_{\alpha\alpha}(\boldsymbol{k}, E)\right], \tag{12}$$

where, based on the Hamiltonian H, the Green's function matrix $\mathbb{G}(\boldsymbol{k}, E)$ would be given by a $M \times M$ matrix as $\mathbb{G}(\boldsymbol{k}, E) = (E - H + \mathrm{i}\eta)^{-1}$, where η is a positive infinitesimal number.

Figure 5 displays the calculated DOS for a ZBLPNR with $M = 12$ (panel (a)) and a ZBLPNR with $M = 16$ (panel (b)) for various electric potentials. When the applied gate voltage is zero ($V = 0$), the DOS shows a sharp peak around zero energy corresponding to zero-edge states compared to bulk states (see insets). Similar to the ZPNR [86], when the applied gate voltage is zero, the local density of states (LDOS) shows a sharp peak around zero energy corresponding to edge states compared to bulk states.

As it is well known, the electrons are confined to a discrete set of energy levels along the $x-$axis. This produces a set of one-dimensional subbands and what are known as van Hove singularities in the density of states for a ZBLPNR, which is an important characteristic of 1D infinitely periodic systems in the density of states at band extrema.

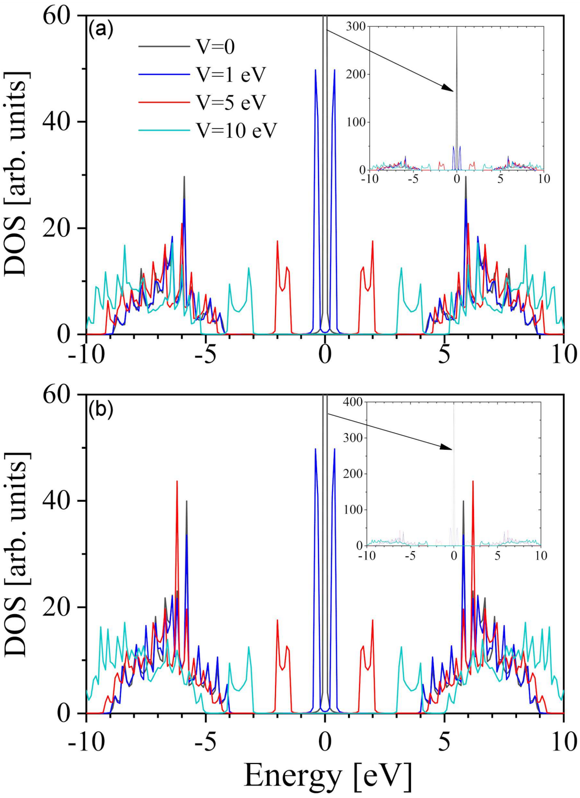

Fig. 5. Densities of states (DOS) calculated for (a) ZBLPNR with $M = 12$ and (b) ZBLPNR with $M = 16$. For better clarity, DOSs around zero energy ($E = 0$) are shown in the insets.

2.2. Tuning the Fermi velocity and effective mass in bilayer phosphorene nanoribbons via an external electric field

Here, we show that the primary transport characteristics of mobile charge carriers, referred to as carrier Fermi velocity and effective mass in bilayer phosphorene nanoribbons, can be effectively tuned by an electric field. Numerous semiconductor physics models (both semi-classical and quantum) are based on the band structure defined by the effective mass parameter [87, 88]. The effective mass calculations derived from the band structure represent the most effective method for accurately predicting the optical and transport properties of semiconductors. In this regard, experiments indicate that, in addition to effective mass, Fermi velocity also plays a crucial role in electronic transport, and by manipulating it, one can control the transport characteristics in semiconductor devices [89]. Furthermore, the potential to modify the Fermi velocity and effective masses of electrons and holes significantly impacts quantum transport measurements [87, 88].

The relationship between band dispersion and charge carrier mobility is formalized through the calculation of effective mass, which, along with scattering time, τ, can be utilized to estimate charge carrier mobility $\mu = e\,\tau/m^*$, determined using the constant relaxation time approximation (CRTA). Consequently, when combined with the carrier density n, the electrical conductivity becomes $\sigma = n\,e^2\tau/m^*$. In the free electron model, the electronic and optical properties typically describe charge carriers as possessing an effective mass m^* and a relaxation time τ. To understand the aforementioned features, we rely on the intuition based on the Drude formula with an effective mass tensor $\sigma \sim 1/m^*$. Thus, calculating the effective mass from band structure calculations is vital for accurately predicting transport.

Its values, however, known from scientific literature for a given semiconductor material, usually differ considerably from one another. Experimentally, the effective masses are usually determined by cyclotron resonance, electro-reflectance measurements, or from analysis of transport data or transport measurements [89].

There are a number of algebraic definitions for the effective mass that can be used to calculate it from the band dispersion relation $E(k)$, which can be obtained, for example, from *ab initio* electronic structure calculations. The influence of the applied electric field on the effective masses of carriers is investigated using the conventional definition of effective mass, which we will refer to as the curvature effective mass. It can be derived alternatively from Newton's second law [90, 91] by discretizing the second time derivative by the second-order derivative of energy with respect to wavevector

$$\frac{1}{m^*} = \frac{1}{\hbar^2}\frac{\partial^2 E}{\partial k^2}. \tag{13}$$

Furthermore, given the band structure described previously, the carrier velocity is calculated by taking the derivative of energy over the wave vector

$$v(k) = \frac{1}{\hbar}\frac{\partial E}{\partial k}. \tag{14}$$

However, it was noted that the effective mass obtained from a particular band structure depends on the approach used to numerically evaluate (13). To compute the derivatives to an arbitrary order of accuracy, one can use a particular conventional scheme, i.e., the finite-difference derivative approximation. A finite difference can be central, forward, or backward. In this regard, the first derivative with a third-order accuracy and the second derivative with a second-order accuracy are as follows [92]

$$\begin{aligned} f'(x_0) &\approx \frac{1}{h}\Big[-\frac{11}{6}f(x_0)+3f(x_1)-\frac{3}{2}f(x_2)+\frac{1}{3}f(x_3)\Big] \\ &\quad + \mathcal{O}(h^3), \\ f''(x_0) &\approx \frac{1}{h^2}\Big[2f(x_0)-5f(x_1)+4f(x_2)-f(x_3)\Big] \\ &\quad + \mathcal{O}(h^2), \end{aligned} \tag{15}$$

in the forward finite difference approximation, where h represents a uniform grid spacing between each finite difference interval, with $x_n = x_0 + nh$.

In low-energy physics, we are often interested in the dispersion of eigenstates close to the conduction or valence band extremum. Figure 6 shows the evolution of the electron velocity in the highest valence band and the lowest conduction band near the Fermi energy for ZBLPNRs with $M = 16$ in the first Brillouin zone, with and without the interlayer hopping parameter t_3. Panel (a) shows the results for zero electric field ($V = 0$), and panel (b) for nonzero electric field ($V = 0.5$ eV). As can be seen, in the absence of the electric field and with t_3 being zero or nonzero, the carrier velocity is zero in a wide region of the first Brillouin zone, which gives rise to localized electronic states in the ZBLPNRs.

We next consider how carrier reciprocal effective mass is varied in the first Brillouin zone of the reciprocal lattice in 1D ZBLPNRs. Figure 7 shows the carrier reciprocal effective mass in the HVB and LCB near the Fermi energy for the ZBLPNRs with $M = 16$ as a function of k between 0 and π/a_x with and without the interlayer hopping t_3. Note that we calculate the effective mass and velocity of the carriers at the band edges, i.e., the conduction band minimum (CBM) and the valence band maximum (VBM). Panel (a) shows the results for zero electric field ($V = 0$), and panel (b) for nonzero electric field ($V = 0.5$ eV).

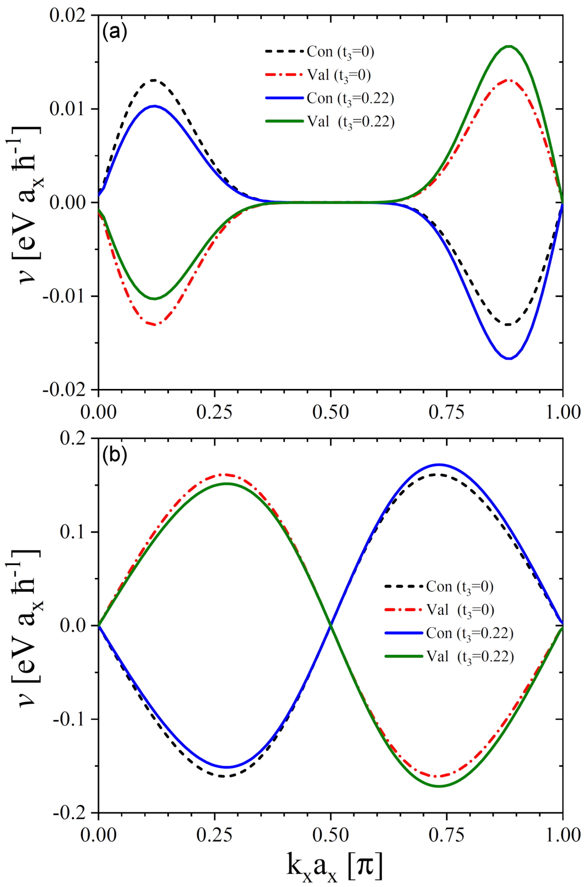

Fig. 6. The electron velocity in the highest valence band and the lowest conduction band near the Fermi energy for ZBLPNRs with $M = 16$ in the first Brillouin zone, with and without the interlayer hopping parameter t_3. Panel (a) shows the result for zero electric field ($V = 0$), and panel (b) for nonzero electric field ($V = 0.5$ eV).

For a better insight into the carrier dynamics in the Brillouin zone of momentum space, we focus on the effective mass and velocity of carriers (Figs. 6b and 7b) simultaneously. For the conduction band (CB) electrons (two solid green curves in Figs. 6b and 7b), if an electron, initially at rest at $k = \pi/a_x$, is accelerated by an electric field, it will move to higher values of k and will become heavier and heavier, reaching infinity at $k = \pi/4a_x$. For even higher values of k, the effective mass becomes negative, heralding the advent of a new particle — the hole. The sign of the effective mass also changes as the carrier charges pass through the point $k = 3\pi/4a_x$. It is worth pointing out that the qualitative trend of the reciprocal effective mass is similar to those obtained for the carrier velocity (see Fig. 6), i.e., in the absence of electric field, regardless of whether t_3 is zero or not, reciprocal effective mass is zero in

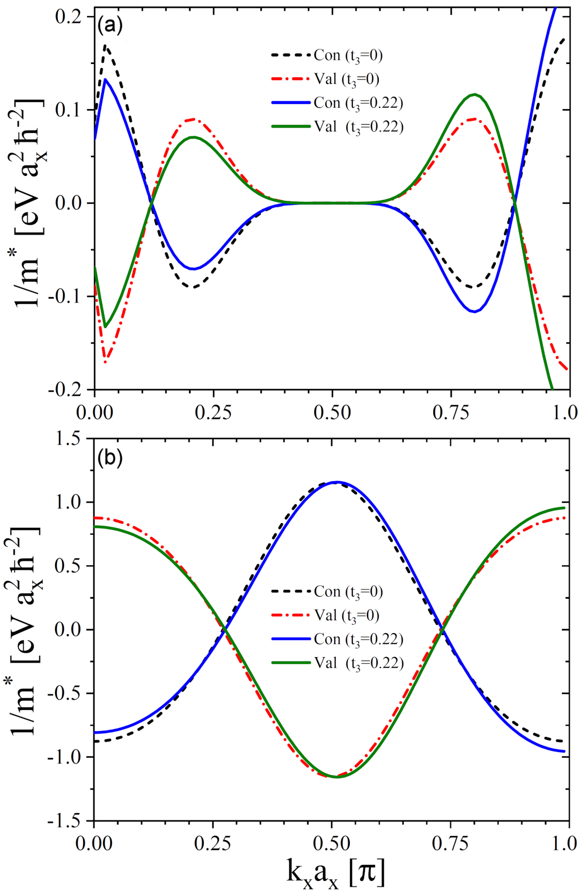

Fig. 7. The carrier reciprocal effective mass in the highest valence band and lowest conduction band near the Fermi energy for ZBLPNRs with $M = 16$ in the first Brillouin zone, with and without the interlayer hopping parameter, t_3. Panel (a) shows the result for zero electric field ($V = 0$), and panel (b) for nonzero electric field ($V = 0.5$ eV).

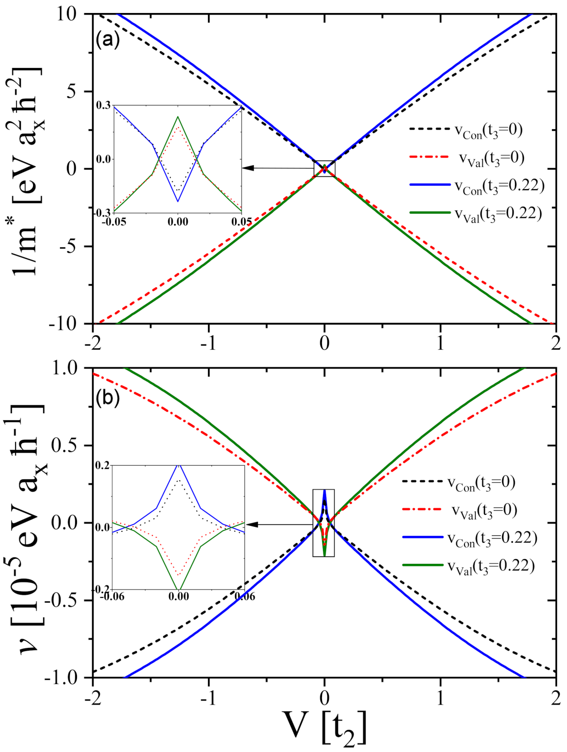

Fig. 8. Reciprocal effective mass (a) and velocity of carriers (b) in the highest valence band and lowest conduction band near the Fermi energy of ZBLPNRs with widths $M = 16$ as a function of the bias voltage.

a wide region of the first Brillouin zone (1st BZ). As a result, we can say, according to the electrical conductivity relation $\sigma = ne^2\tau/m^*$, that in a wide region of the 1st BZ (near the center of the Brillouin zone), the carriers are localized.

To make it more intuitive, we plot the reciprocal effective mass (panel (a)) and velocity of carriers (panel (b)) in the HVB and LCB near the Fermi energy for a ZBLPNR with widths $M = 16$ as a function of the bias voltage. The results are presented in Fig. 8. It is seen that both the Fermi velocity and the reciprocal mass are field-dependent, and therefore, they can be tuned by adjusting an external bias voltage. At certain critical bias voltages ($V_c \sim \pm 0.015$ eV for reciprocal mass and $V_c \sim \pm 0.015$ eV for velocity), regardless of whether t_3 is zero or not, the band edge reciprocal mass and carrier velocity become zero, i.e., the electrons exhibit a localization behavior. For voltages away from the critical bias voltage, both the valence band (VB) and conduction band (CB) show a finite curvature (finite effective mass), allowing the movement of carriers whenever an electric field is applied. However, the critical voltage is the same for both the CBM and VBM, thus, the CBM and VBM wavefunctions are both fully localized over the two layers. Interestingly, for the conduction-band electrons (n-doped sample) or VB holes (p-doped sample) in the limit of zero reciprocal mass (infinite effective mass), the carriers dwelling on that band will be immobile leads to the localization of carriers transporting electrical current, something like Anderson localization of electronic states, but not due to disorder and Coulomb effects on localized charged states. On the other hand, a more important result is the transition from massive (zero velocity) to massless (nonzero velocity) Dirac fermions and vice versa, in the critical bias voltage under a vertical electric field.

It is well known that the Fermi velocity and/or effective mass tunability are distinguishing features of nanoribbons (NRs) that make them particularly promising for many applications. Our approach is a new venue to control both the Fermi velocity and the effective mass of carriers simultaneously in the ZBLPNRs, which is experimentally feasible. Our calculations are in good agreement with the theoretical report of effective masses in black phosphorus [93].

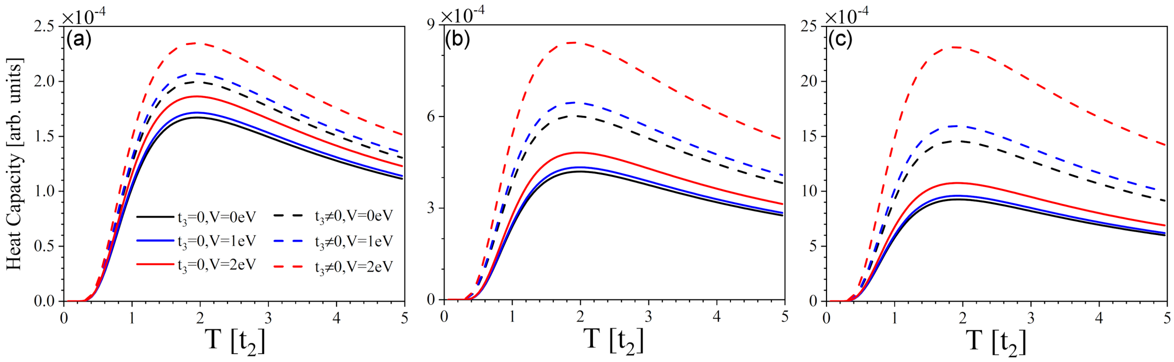

Fig. 9. Heat capacity of a ZBLPNR with $M = 12$ (a), $M = 24$ (b), and $M = 48$ (c) in terms of temperature for several values of electric potential $V = 0, 1, 2$ eV, in the absence ($t_3 = 0$) and presence ($t_3 = 0.22$ eV) of interlayer hopping parameter.

2.3. The orbital magnetic susceptibility and heat capacity in ZBLPNRs

Here, we discuss an important component of magnetic susceptibility — the Pauli paramagnetic susceptibility χ_P. The magnetic moment by the Zeeman effect is

$$\mathcal{M} = \mu_{\rm B}\,(n_\uparrow - n_\downarrow)\,, \tag{16}$$

where $\mu_{\rm B}$ is the Bohr magneton and $n_\uparrow$ ($n_\downarrow$) means the electron density with up-spin (down-spin). The electron density at arbitrary temperature for each spin is given by

$$n_\sigma = \frac{1}{\pi}\int\limits_{\rm 1stBZ} {\rm d}k\,\sum_n \frac{1}{1+{\rm e}^{\beta(\epsilon_{n,k}-\sigma\mu_{\rm B}H)}}, \tag{17}$$

where $\epsilon_{n,k}$ is the sublattice component of the unperturbed eigenvalue, with Bloch momentum k and band index n, where $\sigma(=\uparrow,\downarrow)$ means spin index. Therefore, the Pauli susceptibility χ_P per site is given by

$$\chi_P = \lim_{T\to 0}\frac{\partial\mathcal{M}}{\partial H} = \frac{\beta\,\mu_{\rm B}^2}{\pi\,N_e}\sum_n\int\frac{{\rm d}k}{\cosh\left(\beta\epsilon_{n,k}\right)}, \tag{18}$$

where $\beta = 1/(k_{\rm B}T)$.

For a BLPNR subjected to an electric field, the paramagnetic susceptibility (PPS) and heat capacity (HC) are calculated [94, 95] by energy integrals

$$C(T) = \int\limits_{-\infty}^{\infty}{\rm d}\epsilon\;\epsilon\;D(\epsilon)\,\frac{\partial f(\epsilon,T)}{\partial T}, \tag{19}$$

$$\chi(T) = -\int\limits_{-\infty}^{\infty}{\rm d}\epsilon\;D(\epsilon)\,\frac{\partial f(\epsilon,T)}{\partial\epsilon}, \tag{20}$$

in which $D(\epsilon)$ represents the DOS of electrons and $f(\epsilon,T) = 1/[1+{\rm e}^{\beta(\epsilon-\mu)}]$ is the Fermi distribution function with the chemical potential μ and $\beta = 1/k_{\rm B}T$.

We numerically calculated the finite temperature Pauli susceptibility and electronic heat capacity of zigzag bilayer phosphorene ribbons using these equations up to room temperature and higher. Using (19), (20), and (12), the electronic HC and PPS of the BLPNRs would be calculated, leading to our desired result

$$C(T) = -\frac{1}{4\pi N_c T}\times\sum_\alpha\sum_{\boldsymbol{k}}{\rm Im}\left[\int\limits_{-\infty}^{\infty}{\rm d}\epsilon\;\frac{\epsilon^2\,{\rm e}^{\epsilon/T}}{\left(1+{\rm e}^{\epsilon/T}\right)^2}\mathbb{G}_{\alpha\alpha}(\boldsymbol{k},\epsilon)\right], \tag{21}$$

$$\chi(T) = -\frac{1}{4\pi N_c T}\times\sum_\alpha\sum_\mu\sum_{\boldsymbol{k}}{\rm Im}\left[\int\limits_{-\infty}^{\infty}{\rm d}\epsilon\;\frac{{\rm e}^{\epsilon/T}}{\left(1+{\rm e}^{\epsilon/T}\right)^2}\mathbb{G}_{\alpha\alpha}(\boldsymbol{k},\epsilon)\right]. \tag{22}$$

First of all, it is expected that the Pauli susceptibility and heat capacity of zigzag ribbons might be sensitive to temperature. Figure 9 represents temperature dependent on the heat capacity of the system, namely a ZBLPNR with $M = 12$ (panel (a)), $M = 24$ (panel (b)), and $M = 48$ (panel (c)) in terms of temperature for several values of external electric potential $V = 0, 1, 2$ eV, in the absence ($t_3 = 0$) and presence ($t_3 = 0.22$ eV) of interlayer hopping. It illustrates that all classes exhibit the same behavior with respect to the temperature. The effect of the interlayer hopping term t_3 is also shown. The temperature dependence of the PPS and HC of the ribbons shows that both the PPS and HC increase dramatically with increasing temperature at low temperatures, and after reaching a maximum value, they decrease to a minimum value and remain unchanged at high temperatures, representing a known behavior [95]. Also, it can be observed that PPS increases with the increasing width of the phosphorene ribbons. This thermally assisted electric field control of magnetism opens promising possibilities for thermomagnetic applications based on ZBLPNRs.

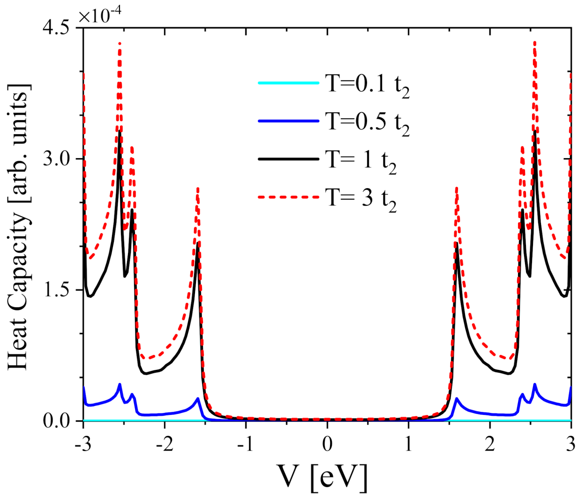

Fig. 10. Heat capacity of a ZBLPNR with $M = 12$ for four finite temperatures $T/t_2 = 0.1, 0.5, 1, 3$, as a function of the electric potential.

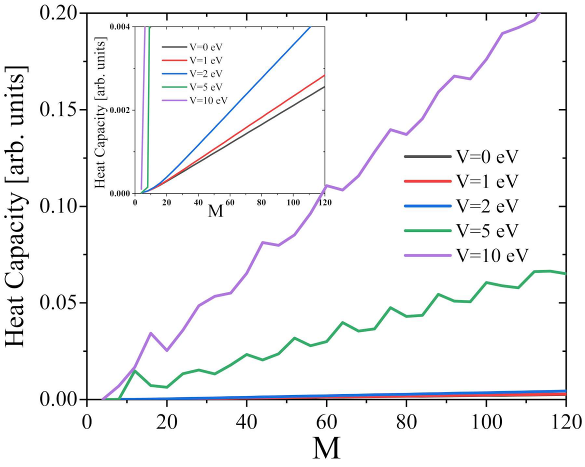

Fig. 11. The width dependence of the HC for ZBLPNRs for several values of electric potential $V = 0, 1, 2, 5, 10$ eV with $T = t_2$.

Furthermore, we explore the tunability of both the PPS and HC using a perpendicular electric field (see Fig. 10). This, in turn, creates the possibility of engineering both the thermal and magnetic properties by tuning an electrical agent through an electric potential difference. As shown in Fig. 10, the quenching of the heat capacity occurs at and below a certain electric potential ($V = \pm 1.25$ eV). This complete suppression of both the PPS and HC using an electric field is another fascinating feature of the devices based on the ZBLPNRs that opens a new way for appealing novel magnetic and thermal control schemes in future low-power-consuming thermomagnetic and spintronic devices. It should be noted that all of these trends are qualitatively established for the case of HC (results for PPS are not shown here).

We further investigate the effect of the nanoribbon width on the HC of ZBLPNRs. The width dependence of the HC at $T = t_2$ for ZBLPNRs, for several values of external electric potential $V = 0$, 1, 2, 5, 10 eV, is shown in Fig. 11. It is clearly seen that HC increases with increasing width of the ribbon. Here again we note that all of these trends are qualitatively established for the case of HC (results for PPS are not shown here).

3. Conclusions

The tight-binding model and Green's function technique have been utilized in order to investigate the electronic, thermal, and magnetic properties of zigzag bilayer phosphorene nanoribbons (ZBLPNRs). A band gap is consistently observed in the energy diagram of ZBLPNRs, characterized by a pair of midgap bands that are completely detached from the bulk bands. The position of the midgap bands can be shifted by applying a perpendicular electric field. This suggests promising potential for modulating the midgap energy bands in zigzag phosphorene nanoribbons for the next generation of semiconductor devices.

The band gap energy of ZBLPNRs depends strongly on the applied electric potential, allowing for the engineering of their electronic properties with desirable characteristics through tuning the external electric field. This leads to a complete and fully reversible metal–to–semiconductor (or insulator) transition that can be readily achieved experimentally. The flexibility of band tunability in ZBLPNRs enhances their potential applications in next-generation optoelectronic nanodevices.

We have also explained the effect of interlayer hopping on the electronic characteristics, specifically the energy band gap, Fermi velocity, and effective mass of carriers in biased bilayer phosphorene nanoribbons. In the presence of interlayer hopping, the low-energy band structure of a ZBLPNR takes the form of two tilted Dirac cones, while in its absence, the two Dirac cones are non-tilted. Moreover, the bands above and below the Fermi level are not symmetric, meaning there is no electron–hole symmetry in the band structures for both limits of the interlayer coupling. Both the Fermi velocity and the reciprocal effective mass become field-dependent, which allows them to be tuned by adjusting the external bias voltage. At certain critical bias voltages, the band edge reciprocal masses and carrier velocities become zero, indicating that the electrons exhibit localization behavior. This phenomenon represents a transition from massive to massless Dirac fermions and vice versa.

Next, we have focused on how the Pauli paramagnetic susceptibility (PPS) and electronic heat capacity (HC) in ZBLPNRs are modified by changing the perpendicular electric field due to the shift in the band structure. The temperature dependence of the PPS and HC of the ribbons shows that both PPS and HC increase dramatically with rising temperature at lower temperatures, reaching a maximum value before declining to a minimum and remaining constant at high temperatures, which reflects a known behavior. Additionally, both PPS and HC increase with increasing ribbon width. A quenching effect on PPS and HC is observed at and below a certain electric field. This approach presents a novel method for simultaneously controlling both the Fermi velocity and effective mass of carriers in ZBLPNRs, which is experimentally feasible. In addition, the ability to control thermal and magnetic properties with an electric field opens up possibilities for thermomagnetic and thermomagnetic applications based on biased ZBLPNRs.

The data that support the findings of the study are available from the corresponding authors upon reasonable request.

Acknowledgments

This work is partially supported by the Iran Science Elites Federation.

References

[1] L. Li, Y. Yu, G.J. Ye, Q. Ge, X. Ou, H. Wu, D. Feng, X.H. Chen, Y. Zhang, *Nat. Nanotechnol.* **9**, 372 (2014).

[2] H. Liu, A.T. Neal, Z. Zhu, Z. Luo, X. Xu, D. Tomanek, P.D. Ye, *ACS Nano* **8**, 4033 (2014).

[3] A. Castellanos-Gomez, *Nat. Photon.* **10**, 202 (2016).

[4] F. Xia, H. Wang, D. Xiao, M. Dubey, A. Ramasubramaniam, *Nat. Photon.* **8**, 899 (2014).

[5] M. Zare, L. Majidi, R. Asgari, *Phys. Rev. B* **96**, 115426 (2017).

[6] A. Carvalho, M. Wang, X. Zhu, A.S. Rodin, H. Su, A.H. Castro Neto, *Nat. Rev. Mater.* **1**, 16061 (2016).

[7] M. Batmunkh, M. Bat-Erdene, J.G. Shapter, *Adv. Mater.* **28**, 8586 (2016).

[8] M. Zare, B.Z. Rameshti, F.G. Ghamsari, R. Asgari, *Phys. Rev. B* **95**, 045422 (2017).

[9] D.-K. Seo, R. Hoffmann, *J. Solid State Chem.* **147**, 26 (1999).

[10] W. Lu, H. Nan, J. Hong, Y. Chen, C. Zhu, Z. Liang, X. Ma, Z. Ni, C. Jin, Z. Zhang, *Nano Res.* **7**, 853 (2014).

[11] X. Wang, A.M. Jones, K.L. Seyler, V. Tran, Y. Jia, H. Zhao, H. Wang, L. Yang, X. Xu, F. Xia, *Nat. Nanotechnol.* **10**, 517 (2015).

[12] H. Liu, Y. Du, Y. Deng, P.D. Ye, *Chem. Soc. Rev.* **44**, 2732 (2015).

[13] S. Das, M. Demarteau, A. Roelofs, *ACS Nano* **8**, 11730 (2014).

[14] M.V. Kamalakar, B.N. Madhushankar, A. Dankert, S.P. Dash, *Small* **11**, 2209 (2015).

[15] R. Fei, L. Yang, *Nano Lett.* **14**, 2884 (2014).

[16] V. Tran, R. Soklaski, Y. Liang, L. Yang, *Phys. Rev. B* **89**, 235319 (2014).

[17] Y. Du, C. Ouyang, S. Shi, M. Lei, *J. Appl. Phys.* **107**, 093718 (2010).

[18] D. Çakir, H. Sahin, F.M. Peeters, *Phys. Rev. B* **90**, 205421 (2014).

[19] L. Liang, J. Wang, W. Lin, B.G. Sumpter, V. Meunier, M. Pan, *Nano Lett.* **14**, 6400 (2014).

[20] A.S. Rodin, A. Carvalho, A.H. Castro Neto, *Phys. Rev. Lett.* **112**, 176801 (2014).

[21] A. Carvalho, A.S. Rodin, A.H. Castro Neto, *Europhys. Lett.* **108**, 47005 (2014).

[22] X. Peng, A. Copple, Q. Wei, *J. Appl. Phys.* **116**, 144301 (2014).

[23] V. Tran, L. Yang, *Phys. Rev. B* **89**, 245407 (2014).

[24] J. Zhang, H.J. Liu, L. Cheng, J. Wei, J.H. Liang, D.D. Fan, J. Shi, X.F. Tang, Q.J. Zhang, *Sci. Rep.* **4**, 6452 (2014).

[25] M. Ezawa, *New J. Phys.* **16**, 115004 (2014).

[26] Q. Wu, L. Shen, M. Yang, Y. Cai, Z. Huang, Y.P. Feng, *Phys. Rev. B* **92**, 035436 (2015).

[27] E.T. Sisakht, M.H. Zare, F. Fazileh, *Phys. Rev. B* **91**, 085409 (2015).

[28] P.M. Das, G. Danda, A. Cupo, W.M. Parkin, L. Liang, N. Kharche, X. Ling, S. Huang, M.S. Dresselhaus, V. Meunier, M. Drndic, *ACS Nano* **10**, 5687, (2016).

[29] M.C. Watts, L. Picco, F.S. Russell-Pavier, P.L. Cullen, T.S. Miller, S.P. Bartuś, O.D. Payton, N.T. Skipper, V. Tileli, C.A. Howard, *Nature* **568**, 216 (2019).

[30] J. He, D. He, Y. Wang, Q. Cui, M.Z. Bellus, H.Y. Chiu, H. Zhao, *ACS Nano* **9**, 6436 (2015).

[31] R.J. Suess, E. Leong, J.L. Garrett, T. Zhou, R. Salem, J.N. Munday, T.E. Murphy, M. Mittendorff, *2D Mater.* **3**, 041006 (2016).

[32] X. Han, H.M. Stewart, S.A. Shevlin, C.R. Catlow, Z.X. Guo, *Nano Lett.* **14**, 4607 (2014).

[33] Z.M. Gibbs, F. Ricci, G. Li, H. Zhu, K. Persson, G. Ceder, G. Hautier, A. Jain, G.J. Snyder, *npj Comput. Mater.* **3**, 8 (2017).

[34] D.C. Elias, R.V. Gorbachev, A.S. Mayorov et al., *Nat. Phys.* **7**, 701 (2011).

[35] C. Attaccalite, A. Rubio, *Phys. Status Solidi B* **246**, 2523 (2009).

[36] F.M.D. Pellegrino, G.G.N. Angilella, R. Pucci, *Phys. Rev. B* **84**, 195404 (2011).

[37] W.-J. Jang, H. Kim, Y.-R. Shin, M. Wang, S.K. Jang, M. Kim, S. Lee, S.-W. Kim, Y.J. Song, S.J. Kahng, *Carbon* **74**, 139 (2014).

[38] A. Díaz-Fernández, L. Chico, J.W. González, F. Domínguez-Adame, *Sci. Rep.* **7**, 8058 (2017).

[39] X. Du, I. Skachko, A. Barker, E.Y. Andrei, *Nat. Nanotechnol.* **3**, 491 (2008).

[40] C.-H. Park, L. Yang, Y.-W. Son, M.L. Cohen, S.G. Louie, *Nat. Phys.* **4**, 213 (2008).

[41] C. Hwang, D.A. Siegel, S.-K. Mo, W. Regan, A. Ismach, Y. Zhang, A. Zettl, A. Lanzara, *Sci. Rep.* **2**, 590 (2012).

[42] J.-H. Yuan, Z. Cheng, Q.-J. Zeng, J.-P. Zhang, J.-J. Zhang, *J. Appl. Phys.* **110**, 103706 (2011).

[43] A. Raoux, M. Polini, R. Asgari, A.R. Hamilton, R. Fazio, A.H. MacDonald, *Phys. Rev. B* **81**, 073407 (2010).

[44] J.R.F. Lima, *Phys. Lett. A* **379**, 179 (2015).

[45] J.R.F. Lima, A.L. Barbosa, C. Bezerra, L.F.C. Pereira, *Phys. E: Low-dimen. Syst. Nanostruct.* **97**, 105 (2018).

[46] F. Sattari, S. Mirershadi, *Superlattices Microstruct.* **111**, 438 (2017).

[47] A.R.S. Lins, J.R.F. Lima, *Carbon* **160**, 353 (2020).

[48] P. Ghosh, P. Roy, *Eur. Phys. J. Plus* **132**, 32 (2017).

[49] S. Lee, F. Yang, J. Suh et al., *Nat. Commun.* **6**, 8573 (2015).

[50] H. Mousavi, J. Khodadadi, *Superlattices Microstruct.* **88**, 434 (2015).

[51] D. Çakır, C. Sevik, F.M. Peeters, *Phys. Rev. B* **92**, 165406 (2015).

[52] B. Jhun, C.-H. Park, *Phys. Rev. B* **96**, 085412 (2017).

[53] L.L. Li, D. Moldovan, W. Xu, F.M. Peeters, *Phys. Rev. B* **96**, 155425 (2017).

[54] A.N. Rudenko, S. Yuan, M.I. Katsnelson, *Phys. Rev. B* **92**, 085419 (2016).

[55] K. Dolui, S. Quek, *Sci. Rep.* **5**, 11699 (2015).

[56] S. Yuan, E. van Veen, M.I. Katsnelson, R. Roldán, *Phys. Rev. B* **93**, 245433 (2016).

[57] D. Zhang, W. Lou, M. Miao, S.-C. Zhang, K. Chang, *Phys. Rev. Lett.* **111**, 156402 (2013).

[58] B. Deng, V. Tran, Y. Xie et al., *Nat. Comun.* **8**, 14474 (2017).

[59] T.-N. Do, P.-H. Shih, G. Gumbs, D. Huang, *Phys. Rev. B* **103**, 115408 (2021).

[60] M. Zare, E. Sadeghi, *Phys. Rev. B* **98**, 205401 (2018).

[61] A. Maity, A. Singh, P. Sen, A. Kibey, A. Kshirsagar, D.G. Kanhere, *Phys. Rev. B* **94**, 075422 (2016).

[62] E. Taghizadeh Sisakht, M.H. Zare, F. Fazileh, *Phys. Rev. B* **91**, 085409 (2015).

[63] R. Ma, H. Geng, W.Y. Deng, M.N. Chen, L. Sheng, D.Y. Xing, *Phys. Rev. B* **94**, 125410 (2016).

[64] B. Ostahie, A. Aldea, *Phys. Rev. B* **93**, 075408 (2015).

[65] B. Zhou, B. Zhou, X. Zhou, G. Zhou, *J. Phys. D Appl. Phys.* **50**, 045106 (2017).

[66] L. Yang, W. Mi, X. Wang, *J. Alloys Compd.* **662**, 528 (2016).

[67] H. Zhang, Y. Li, J. Hou, A. Du, Z. Chen, *Nano Lett.* **16**, 6124 (2016).

[68] A. Carvalho, A. Rodin, A.C. Neto, *Europhys. Lett.* **108**, 47005 (2014).

[69] H. Guo, N. Lu, J. Da, X. Wu, X.C. Zeng, *J. Phys. Chem. C* **118**, 14051 (2014).

[70] T. Mertz, P. Wunderlich, S. Bhattacharyya, F. Ferrari, R. Valentí, *npj Comput. Mater.* **8**, 66 (2022).

[71] K. Liu, L. Zhang, T. Cao, C. Jin, D. Qiu, Q. Zhou, A. Zettl, P. Yang, S.G. Louie, F. Wang, *Nat. Commun.* **5**, 4966 (2014).

[72] N. Xuan, A. Xie, B. Liu, Z. Sun, *Carbon* **201**, 529 (2023).

[73] C. Weeks, M. Franz, *Phys. Rev. B* **82**, 085310 (2010).

[74] D. Geng, H. Zhou, S. Yue, Z. Sun, P. Cheng, L. Chen, S. Meng, K. Wu, B. Feng, *Nat. Commun.* **13**, 7000 (2022).

[75] L. Meng, W. Yan, Z.-D. Chu, Y. Zhang, L. Feng, R.-F. Dou, J.-C. Nie, L. He, arXiv:1208.0903, 2012.

[76] L. Meng, Y. Zhang, W. Yan, L. Feng, L. He, R.-F. Dou, J.-C. Nie, *Appl. Phys. Lett.* **100**, 091601 (2012).

[77] L. Meng, W. Yan, L. Yin, Z.-D. Chu, Y. Zhang, L. Feng, R. Dou, J. Nie, *J. Phys. Chem. C* **118**, 6462 (2014).

[78] N. Zhu, J. Jiang, A. Zafar, J. Hong, Y. Zhang, *APL Mater.* **7**, 041108 (2019).

[79] T. Salamon, B. Irsigler, D. Rakshit, M. Lewenstein, T. Grass, R. Chhajlany, *Phys. Rev. B* **106**, 174503 (2022).

[80] D.O. Oriekhov, V.P. Gusynin, V.M. Loktev, *Phys. Rev. B* **103**, 195104 (2021).

[81] D. Sénéchal, A.-M.S. Tremblay, *Phys. Rev. Lett.* **92**, 126401 (2004).

[82] M. Civelli, M. Capone, S.S. Kancharla, O. Parcollet, G. Kotliar, *Phys. Rev. Lett.* **95**, 106402 (2005).

[83] W. Wu, M.S. Scheurer, M. Ferrero, A. Georges, *Phys. Rev. Research* **2**, 033067 (2020).

[84] M. Zare, *Supercond. Sci. Technol.* **32**, 115002 (2019).

[85] S.-M. Choi, S.-H. Jhi, Y.-W. Son, *Phys. Rev. B* **81**, 081407(R) (2010).

[86] S.F. Islam, P. Dutta, A.M. Jayannavar, A. Saha, *Phys. Rev. B* **97**, 235424 (2018).

[87] D.L. Rode, *Semiconductors and Semimetals, Transport Phenomena*, Vol. 10, Academic Press, New York 1975, p. 1.

[88] W.A. Harrison, *Electronic Structure and the Properties of Solids*, W.H. Freeman and Company, San Francisco 1980.

[89] O. Zakharov, A. Rubio, X. Blase, M.L. Cohen S.G. Louie, *Phys. Rev. B* **50**, 10780 (1994).

[90] N. Ashcroft, N. Mermin, *Solid State Physics*, Saunders College, Philadelphia 1976.

[91] V. Ariel, arXiv:1205.3995, 2012.

[92] B. Fornberg, *Math. Comput.* **51**, 699 (1988).

[93] C. Sevik, J.R. Wallbank, O. Gülseren, F.M. Peeters, D. Çakır, *2D Mater.* **4**, 035025 (2017).

[94] W. Nothing, A. Ramakanth, *Quantum Theory of Magnetism*, Springer, New York 2009.

[95] H. Mousavi, *J. Magn. Magn. Mater.* **322**, 2533 (2010).